Journal of
Marine Science and Engineering

MDPI

Article

An Analytical Symplectic Method for Buckling of Ring-Stiffened Graphene Platelet-Reinforced Composite Cylindrical Shells Subjected to Hydrostatic Pressure

Zhanzhong Sun [1], Gangyi Hu [1], Xueyang Nie [2] and Jiabin Sun [3,*]

[1] China Ship Development and Design Center, Wuhan 430064, China
[2] State Key Laboratory of Structure Analysis of Industrial Equipment and Department of Engineering Mechanics, Dalian University of Technology, Dalian 116024, China
[3] State Key Laboratory of Structural Analysis of Industrial Equipment and School of Ocean Science and Technology, Dalian University of Technology, Panjin 124221, China
* Correspondence: jbsun1983@dlut.edu.cn; Tel.: +86-135-0411-3865

Abstract: In this paper, a novel analytical approach for the buckling of ring-stiffened porous graphene platelet-reinforced composite cylindrical shells under hydrostatic pressure is proposed under the framework of symplectic mechanics. Three types of graphene platelet-reinforced patterns and porosity distributions are considered, and the effective material properties of porous graphene platelet-reinforced composite are determined with a modified Halpin–Tsai model. In the symplectic approach, the governing equations in the conventional Lagrangian system are transformed into a set of Hamiltonian canonical equations, and therefore, the buckling analysis is reduced into an eigenproblem in a symplectic space. Consequently, the accurate critical pressures and corresponding analytical buckling mode shapes are obtained simultaneously without any trial function. The numerical results are compared with the existing results, and good agreements are observed. A comprehensive parametric study of the geometrical parameters, boundary conditions, material properties, and ring-stiffener parameters on the buckling behavior of such shells is also presented.

Keywords: symplectic method; critical load; cylindrical shell; buckling; hydrostatic pressure

Citation: Sun, Z.; Hu, G.; Nie, X.; Sun, J. An Analytical Symplectic Method for Buckling of Ring-Stiffened Graphene Platelet-Reinforced Composite Cylindrical Shells Subjected to Hydrostatic Pressure. *J. Mar. Sci. Eng.* **2022**, *10*, 1834. https://doi.org/10.3390/jmse10121834

Academic Editors: Joško Parunov and Yordan Garbatov

Received: 19 October 2022
Accepted: 20 November 2022
Published: 29 November 2022

1. Introduction

Ring-stiffened cylindrical shell structures are widely used in military submarines, underwater pipelines, sightseeing submersibles, etc. [1]. The buckling instability is one of the most important failure modes because these devices are usually subjected to hydrostatic pressure. Therefore, it is of great importance to perform the buckling analysis of such ring-stiffened cylindrical shells under hydrostatic pressure.

Plenty of theoretical, numerical, and experimental studies on the stability of ring-stiffened cylindrical shells have been carried out in the past decades. Kendrick [2] and Bryant [3] derived the empirical formulas for the critical pressure of simply-supported ring-stiffened cylindrical shells under hydrostatic pressure. Galletly et al. [4] and Yamamoto et al. [5] performed experiments on the general stability of ring-stiffened cylindrical shells under hydrostatic pressure. Rathinam et al. [6] performed a finite element analysis of the buckling of ring-stiffened cylindrical shells under external pressure using ANSYS. Baruch and Singer [7] and Reddy and Starnes [8] proposed the analytical solution for the general instability of simply supported stiffened cylindrical shells under hydrostatic pressure using the Naiver solution. Shen [9,10] investigated the post-buckling of stiffened cylindrical shells under combined external pressure and axial compression/thermal loading using the singular perturbation technique. The buckling of ring-stiffened cylindrical shells under external pressure has also been investigated using energy methods, such as the Ritz method [11–13] and the Galerkin method [14–16].

In view of the above literature, the existing research on ring-stiffened cylindrical shells has mainly been concentrated on homogeneous metal material. In recent years, much progress has been made in the rapid development of composites, and more and more nanocomposites with excellent mechanical properties have been fabricated [17–22]. Graphene platelet-reinforced composite (GPLRC) is one of the very promising nano-reinforced composites [23–25]. Graphene platelet is one of the derivatives of graphene and is formed by several layers of graphene with a thickness of up to 100 nm. There is evidence that the addition of a very small number of GPLs into a metal matrix can dramatically improve its mechanical properties [26–28]. At the current stage, the buckling of GPLRC cylindrical shells has been reported in the open literature. Liu et al. [29] investigated the buckling of FG GPLRC cylindrical shells under initial axial stress by the state–space formulation. Zhao et al. [30] and Sun et al. [31] investigated the axial buckling and torsional buckling of FG GPLRC cylindrical shells using the symplectic method. Zhou et al. [32], Dong et al. [33], and Sun et al. [34] investigated the buckling and post-buckling of FG GPLRC cylindrical shells under axial compression using the Galerkin method. Blooriyan et al. [35] and Shahgholian-Ghahfarokhi et al. [36–38] studied the buckling of FG GPLRC cylindrical shells subject to axial compression and lateral pressure using the Ritz method Wang et al. [39–41] investigated the buckling of GPLRC cylindrical shells with cutouts under axial compression and torsion using the finite element method.

From the above literature summary, it was found that two major limitations exist:

(i) The existing research on the buckling of GPLRC cylindrical shells is mainly concentrated on axial compression, and external pressure is rarely mentioned. Moreover, the buckling of ring-stiffened porous GPLRC cylindrical shells under hydrostatic pressure has not been mentioned in the open literature;

(ii) The existing theoretical research is mainly based on the energy method, which requires some pre-determined trial functions. However, it is difficult to obtain the proper trial functions for different boundary conditions and load forms. Therefore, it is necessary to propose a rational and rigorous analytical method for the buckling of ring-stiffened porous GPLRC cylindrical shells.

Motivated by these reasons, we proposed a novel analytical symplectic method to find exact solutions for the buckling of ring-stiffened porous GPLRC cylindrical shells under hydrostatic pressure. The symplectic methodology has been proven to be an effective way to resolve some basic problems in solid mechanics which have long been challenges [42,43]. Compared to numerical methods, such as the finite element method and the differential quadrature method [44–46], it does not need to perform discrete processing. The solution has analytical expressions and higher computational efficiency. Compared to the Navier solution [47,48], it does not need to assume an approximate displacement function and can handle different boundary conditions. In the framework of symplectic mechanics, the governing equations in the conventional solution system are transformed into Hamiltonian form. Consequently, the accurate critical hydrostatic pressure and buckling mode are obtained without any trial functions. Key influencing factors on the buckling behavior of ring-stiffened porous GPLRC cylindrical shells are investigated and discussed. The main innovation of this paper is to propose an analytical method for the buckling analysis of ring-stiffened composite cylindrical shells under hydrostatic pressure and obtain accurate critical loads and buckling modes. The proposed method and obtained results can provide a theoretical basis and guidance for the stability design of ring-stiffened composite cylindrical shells, which can be applied to submarines, underwater pipelines, sightseeing submersibles, and other marine engineering structures.

This paper is organized as follows: the mathematical modeling of ring-stiffened porous GPLRC cylindrical shells is present in Section 2. Section 3 presents the Hamilton system and solving procedure. The effective material properties of porous GPLRC are given in Section 4. Numerical examples are provided in Section 5. Finally, the contributions are summarized in Section 6.

2. Mathematical Modeling of Ring-Stiffened Porous GPLRC Cylindrical Shells

Consider a ring-stiffened porous GPLRC cylindrical shell under hydrostatic pressure P, as shown in Figure 1. The shell and ring-stiffeners are made of metal matrix GPLRC composite and pure metal, respectively. The geometry of the shell is the length L, thickness h, and radius of the mid-plane R. The ring-stiffener spacing is L_F. The height and width of the ring-stiffener are h_F and d_F, respectively. The shell is referred to as a coordinate system (x, θ, z), where x-, θ-, and z- represent the longitudinal, circumferential, and normal of the shell, respectively. The displacements of the mid-plane along the x-, θ-, and z-axes are u, v, and w, respectively.

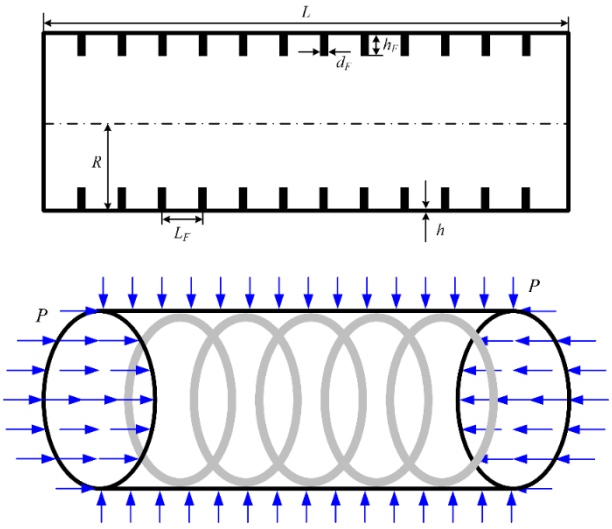

Figure 1. Schematic of ring-stiffened porous GPLRC cylindrical shell under hydrostatic pressure.

For the mechanical behaviors of the beam, plate, and shell structures, the high-order shear deformation theory [49–53], considering the transverse shear deformation, is more accurate. This paper mainly focuses on thin-walled shells whose h/R is less than 1/50. In this case, the Kirchhoff–Love hypothesis can obtain a sufficiently accurate solution. In order to simplify the theoretical model and solution process, the Kirchhoff–Love hypothesis is used in this paper. The strain of arbitrary point on the shell can be expressed as [13]

$$\varepsilon_x = \varepsilon_x^{(0)} + z\chi_x \tag{1}$$

$$\varepsilon_\theta = \varepsilon_\theta^{(0)} + z\chi_\theta \tag{2}$$

$$\gamma_{x\theta} = \gamma_{x\theta}^{(0)} + z\chi_{x\theta} \tag{3}$$

where $\varepsilon_x^{(0)}$, $\varepsilon_\theta^{(0)}$, and $\gamma_{x\theta}^{(0)}$ are the strain components on the mid-plane of the shell, and χ_x, χ_θ, and $\chi_{x\theta}$ are the curvature.

According to Donnell's shell theory, the relations between the strain and the curvature are expressed as [13]

$$\varepsilon_x^{(0)} = \frac{\partial u}{\partial x} \tag{4}$$

$$\varepsilon_\theta^{(0)} = \frac{\partial v}{R\partial\theta} + \frac{w}{R} \tag{5}$$

$$\gamma_{x\theta}^{(0)} = \frac{\partial u}{R\partial\theta} + \frac{\partial v}{\partial x} \tag{6}$$

$$\chi_x = -\frac{\partial^2 w}{\partial x^2} \tag{7}$$

$$\chi_\theta = -\frac{\partial^2 w}{R^2 \partial \theta^2} \tag{8}$$

$$\chi_{x\theta} = -2\frac{\partial^2 w}{R \partial x \partial \theta} \tag{9}$$

The constitutive equation of the porous GPLRC cylindrical shells can be written as [16]

$$\begin{Bmatrix} \sigma_x \\ \sigma_\theta \\ \tau_{x\theta} \end{Bmatrix} = \begin{bmatrix} c_{11} & c_{12} & 0 \\ c_{12} & c_{22} & 0 \\ 0 & 0 & c_{66} \end{bmatrix} \begin{Bmatrix} \varepsilon_x \\ \varepsilon_\theta \\ \gamma_{x\theta} \end{Bmatrix} \tag{10}$$

where σ_x, σ_θ, and $\tau_{x\theta}$ are the stress components of an arbitrary point on the shell, and $c_{11} = c_{22} = E_s/\left(1-\nu_s^2\right)$, $c_{12} = E_s\nu_s/\left(1-\nu_s^2\right)$, $c_{66} = E_s/[2(1+\nu_s)]$, E_s, and ν_s are the Young's modulus and Poisson's ratio of the shell.

The inner force and moment of the ring-stiffened porous GPLRC cylindrical shells are expressed as [16]

$$N_x = \int_{-h/2}^{h/2} \sigma_x dz \tag{11}$$

$$N_\theta = \int_{-h/2}^{h/2} \sigma_\theta dz + F_{11}\varepsilon_\theta^{(0)} + F_{12}\chi_\theta \tag{12}$$

$$N_{x\theta} = \int_{-h/2}^{h/2} \tau_{x\theta} dz \tag{13}$$

$$M_x = \int_{-h/2}^{h/2} \sigma_x z dz \tag{14}$$

$$M_\theta = \int_{-h/2}^{h/2} \sigma_\theta z dz + F_{12}\varepsilon_\theta^{(0)} + F_{22}\chi_\theta \tag{15}$$

$$M_{x\theta} = \int_{-h/2}^{h/2} \tau_{x\theta} z dz \tag{16}$$

where $F_{11} = E_F A_F/L_F$, $F_{12} = E_F A_F e/L_F$, $F_{22} = E_F\left(I_F + A_F e^2\right)/L_F$, and $I_F = d_F h_F^3/12$, E_F are the Young's modulus values of the ring-stiffener, A_F is the section area of the ring-stiffener, and e is the eccentric distance of the ring-stiffener.

When substituting Equations (1)–(10) into Equations (11)–(16), the expression of the resultant forces and moments can be written as [16]

$$N_x = A_{11}\varepsilon_x^{(0)} + A_{12}\varepsilon_\theta^{(0)} + B_{11}\chi_x + B_{12}\chi_\theta \tag{17}$$

$$N_\theta = A_{12}\varepsilon_x^{(0)} + (A_{22}+F_{11})\varepsilon_\theta^{(0)} + B_{12}\chi_x + (B_{22}+F_{12})\chi_\theta \tag{18}$$

$$N_{x\theta} = A_{66}\varepsilon_{x\theta}^{(0)} + B_{66}\chi_{x\theta} \tag{19}$$

$$M_x = B_{11}\varepsilon_x^{(0)} + B_{12}\varepsilon_\theta^{(0)} + D_{11}\chi_x + D_{12}\chi_\theta \tag{20}$$

$$M_\theta = B_{12}\varepsilon_x^{(0)} + (B_{22}+F_{12})\varepsilon_\theta^{(0)} + D_{12}\chi_x + (D_{22}+F_{22})\chi_\theta \tag{21}$$

$$M_{x\theta} = B_{66}\varepsilon_{x\theta}^{(0)} + D_{66}\chi_{x\theta} \tag{22}$$

where $A_{ij} = \int_{-h/2}^{h/2} c_{ij} dz$, $B_{ij} = \int_{-h/2}^{h/2} c_{ij} z dz$, $D_{ij} = \int_{-h/2}^{h/2} c_{ij} z^2 dz$.

The strain energy density of the ring-stiffened porous GPLRC cylindrical shells is

$$\begin{aligned} \Pi_E &= \tfrac{1}{2}\left(N_x\varepsilon_x^{(0)} + N_\theta\varepsilon_\theta^{(0)} + N_{x\theta}\gamma_{x\theta}^{(0)} + M_x\chi_x + M_\theta\chi_\theta + M_{x\theta}\chi_{x\theta}\right) \\ &= \tfrac{1}{2}\left\{\begin{array}{l} A_{11}\left(\frac{\partial u}{\partial x}\right)^2 + 2A_{12}\left(\frac{\partial u}{\partial x}\right)\left(\frac{\partial v}{R\partial\theta} + \frac{w}{R}\right) + (A_{22}+F_{11})\left(\frac{\partial v}{R\partial\theta} + \frac{w}{R}\right)^2 \\ +A_{66}\left(\frac{\partial u}{R\partial\theta} + \frac{\partial v}{\partial x}\right)^2 - 2B_{11}\left(\frac{\partial u}{\partial x}\right)\left(\frac{\partial^2 w}{\partial x^2}\right) - 2B_{12}\left(\frac{\partial v}{R\partial\theta} + \frac{w}{R}\right)\left(\frac{\partial^2 w}{\partial x^2}\right) \\ -2B_{12}\left(\frac{\partial u}{\partial x}\right)\left(\frac{\partial^2 w}{R^2\partial\theta^2}\right) - 2(B_{22}+F_{12})\left(\frac{\partial v}{R\partial\theta} + \frac{w}{R}\right)\left(\frac{\partial^2 w}{R^2\partial\theta^2}\right) \\ -4B_{66}\left(\frac{\partial u}{R\partial\theta} + \frac{\partial v}{\partial x}\right)\left(\frac{\partial^2 w}{R\partial x\partial\theta}\right) + D_{11}\left(\frac{\partial^2 w}{\partial x^2}\right)^2 + 2D_{12}\left(\frac{\partial^2 w}{\partial x^2}\right)\left(\frac{\partial^2 w}{R^2\partial\theta^2}\right) \\ +(D_{22}+F_{22})\left(\frac{\partial^2 w}{R^2\partial\theta^2}\right)^2 + 4D_{66}\left(\frac{\partial^2 w}{R\partial x\partial\theta}\right)^2 \end{array}\right\} \end{aligned} \tag{23}$$

The expression of the external force work density under hydrostatic pressure is

$$\Pi_W = \frac{1}{2}N_x^0\left(\frac{\partial w}{\partial x}\right)^2 + \frac{1}{2}N_\theta^0\left(\frac{\partial w}{R\partial\theta}\right)^2 \tag{24}$$

where $N_x^0 = -PR/2$ and $N_\theta^0 = -PR$.

3. Hamilton System and Solving Procedure

To establish the Hamilton system for the buckling of the ring-stiffened porous GPLRC cylindrical shell, the circumferential coordinate θ is simulated as the time coordinate [54], and, therefore, the Lagrangian function can be expressed as

$$\begin{aligned} L(u,v,w,\Phi) &= \tfrac{1}{2}N_x^0\left(\tfrac{\partial w}{\partial x}\right)^2 + \tfrac{1}{2}N_\theta^0\Phi^2 \\ &+\tfrac{1}{2}\left\{\begin{array}{l} A_{11}\left(\frac{\partial u}{\partial x}\right)^2 + 2A_{12}\left(\frac{\partial u}{\partial x}\right)\left(\frac{\dot v}{R} + \frac{w}{R}\right) + (A_{22}+F_{11})\left(\frac{\dot v}{R} + \frac{w}{R}\right)^2 \\ +A_{66}\left(\frac{\dot u}{R} + \frac{\partial v}{\partial x}\right)^2 - 2B_{11}\left(\frac{\partial u}{\partial x}\right)\left(\frac{\partial^2 w}{\partial x^2}\right) - 2B_{12}\left(\frac{\dot v}{R} + \frac{w}{R}\right)\left(\frac{\partial^2 w}{\partial x^2}\right) \\ -2B_{12}\left(\frac{\partial u}{\partial x}\right)\left(\frac{\dot\Phi}{R}\right) - 2(B_{22}+F_{12})\left(\frac{\dot v}{R} + \frac{w}{R}\right)\left(\frac{\dot\Phi}{R}\right) \\ -4B_{66}\left(\frac{\dot u}{R} + \frac{\partial v}{\partial x}\right)\left(\frac{\partial\Phi}{\partial x}\right) + D_{11}\left(\frac{\partial^2 w}{\partial x^2}\right)^2 + 2D_{12}\left(\frac{\partial^2 w}{\partial x^2}\right)\left(\frac{\dot\Phi}{R}\right) \\ +(D_{22}+F_{22})\left(\frac{\dot\Phi}{R}\right)^2 + 4D_{66}\left(\frac{\partial\Phi}{\partial x}\right)^2 \end{array}\right\} \end{aligned} \tag{25}$$

where $\dot f = \partial f/\partial\theta$, and $\Phi = -\partial w/(R\partial\theta) = -\dot w/R$ is the angle of rotation.

Define the original vector as

$$\mathbf{q} = \{u, v, w, \Phi\}^{\mathrm{T}} \tag{26}$$

Its dual vector can be obtained by $\mathbf{p} = \delta L/\delta\dot{\mathbf{q}} = \{P_1, P_2, P_3, P_4\}^{\mathrm{T}}$, where

$$P_1 = \frac{\delta L}{\delta\dot u} = A_{66}\left(\frac{\dot u}{R} + \frac{\partial v}{\partial x}\right) + 2B_{66}\frac{\partial\Phi}{\partial x} \tag{27}$$

$$P_2 = \frac{\delta L}{\delta\dot v} = A_{12}\frac{\partial u}{\partial x} + (A_{22}+F_{11})\left(\frac{\dot v}{R} + \frac{w}{R}\right) - B_{12}\frac{\partial^2 w}{\partial x^2} + (B_{22}+F_{12})\frac{\dot\Phi}{R} \tag{28}$$

$$P_3 = \frac{\delta L}{\delta\dot w} = \dot P_4 \tag{29}$$

$$P_4 = \frac{\delta L}{\delta\dot\Phi} = (D_{22}+F_{22})\frac{\dot\Phi}{R} - D_{12}\frac{\partial^2 w}{\partial x^2} + B_{12}\frac{\partial u}{\partial x} + (B_{22}+F_{12})\left(\frac{\dot v}{R} + \frac{w}{R}\right) \tag{30}$$

By means of Equations (26) and (27), the governing equations for the buckling of the ring-stiffened porous GPLRC cylindrical shells can be represented in the Hamiltonian form

$$\dot{u} = -R\frac{\partial v}{\partial x} - \frac{2RB_{66}}{A_{66}}\frac{\partial \Phi}{\partial x} + \frac{R}{A_{66}}P_1 \tag{31}$$

$$\begin{aligned}\dot{v} = &\frac{R[B_{12}(B_{22}+F_{12}) - A_{12}(D_{22}+F_{22})]}{(A_{22}+F_{11})(D_{22}+F_{22}) - (B_{22}+F_{12})^2}\frac{\partial u}{\partial x} + \frac{R[B_{12}(D_{22}+F_{22}) - D_{12}(B_{22}+F_{12})]}{(A_{22}+F_{11})(D_{22}+F_{22}) - (B_{22}+F_{12})^2}\frac{\partial^2 w}{\partial x^2}\\ &-w + \frac{R(D_{22}+F_{22})}{(A_{22}+F_{11})(D_{22}+F_{22}) - (B_{22}+F_{12})^2}P_2 - \frac{R(B_{22}+F_{12})}{(A_{22}+F_{11})(D_{22}+F_{22}) - (B_{22}+F_{12})^2}P_4\end{aligned} \tag{32}$$

$$\dot{w} = -R\Phi \tag{33}$$

$$\begin{aligned}\dot{\Phi} = &\frac{R[A_{12}(B_{22}+F_{12}) - B_{12}(A_{22}+F_{11})]}{(A_{22}+F_{11})(D_{22}+F_{22}) - (B_{22}+F_{12})^2}\frac{\partial u}{\partial x} + \frac{R[D_{12}(A_{22}+F_{11}) - B_{12}(B_{22}+F_{12})]}{(A_{22}+F_{11})(D_{22}+F_{22}) - (B_{22}+F_{12})^2}\frac{\partial^2 w}{\partial x^2}\\ &-\frac{R(B_{22}+F_{12})}{(A_{22}+F_{11})(D_{22}+F_{22}) - (B_{22}+F_{12})^2}P_2 + \frac{R(A_{22}+F_{11})}{(A_{22}+F_{11})(D_{22}+F_{22}) - (B_{22}+F_{12})^2}P_4\end{aligned} \tag{34}$$

$$\begin{aligned}\dot{P}_1 = &R\left[\frac{B_{12}^2(A_{22}+F_{11}) - 2A_{12}B_{12}(B_{22}+F_{12}) + A_{12}^2(D_{22}+F_{22})}{(A_{22}+F_{11})(D_{22}+F_{22}) - (B_{22}+F_{12})^2} - A_{11}\right]\frac{\partial^2 u}{\partial x^2}\\ &+R\frac{A_{12}D_{12}(B_{22}+F_{12}) - B_{12}D_{12}(A_{22}+F_{11}) - A_{12}B_{12}(D_{22}+F_{22}) + B_{12}^2(B_{22}+F_{12})}{(A_{22}+F_{11})(D_{22}+F_{22}) - (B_{22}+F_{12})^2}\frac{\partial^3 w}{\partial x^3}\\ &+\frac{R[A_{12}(D_{22}+F_{22}) - B_{12}(B_{22}+F_{12})]}{(A_{22}+F_{11})(D_{22}+F_{22}) - (B_{22}+F_{12})^2}\frac{\partial P_2}{\partial x} + \frac{R[A_{12}(B_{22}+F_{12}) - B_{12}(A_{22}+F_{11})]}{(A_{22}+F_{11})(D_{22}+F_{22}) - (B_{22}+F_{12})^2}\frac{\partial P_4}{\partial x}\end{aligned} \tag{35}$$

$$\dot{P}_2 = -R\frac{\partial P_1}{\partial x} \tag{36}$$

$$\begin{aligned}\dot{P}_3 = &R\frac{B_{12}D_{12}(A_{22}+F_{11}) - A_{12}D_{12}(B_{22}+F_{12}) + A_{12}B_{12}(D_{22}+F_{22}) - B_{12}^2(B_{22}+F_{12})}{(A_{22}+F_{11})(D_{22}+F_{22}) - (B_{22}+F_{12})^2}\frac{\partial^3 u}{\partial x^3}\\ &-R\left[\frac{B_{12}^2(D_{22}+F_{22}) - 2B_{12}D_{12}(B_{22}+F_{12}) + D_{12}^2(A_{22}+F_{11})}{(A_{22}+F_{11})(D_{22}+F_{22}) - (B_{22}+F_{12})^2} + D_{11}\right]\frac{\partial^4 w}{\partial x^4} + RN_x^0\frac{\partial^2 w}{\partial x^2} - P_2\\ &+\frac{R[D_{12}(B_{22}+F_{12}) - B_{12}(D_{22}+F_{22})]}{(A_{22}+F_{11})(D_{22}+F_{22}) - (B_{22}+F_{12})^2}\frac{\partial^2 P_2}{\partial x^2} + \frac{R[B_{12}(B_{22}+F_{12}) - D_{12}(A_{22}+F_{11})]}{(A_{22}+F_{11})(D_{22}+F_{22}) - (B_{22}+F_{12})^2}\frac{\partial^2 P_4}{\partial x^2}\end{aligned} \tag{37}$$

$$\dot{P}_4 = -4RD_{66}\frac{\partial^2 \Phi}{\partial x^2} - \frac{2RB_{66}}{A_{66}}\frac{\partial P_1}{\partial x} + RP_3 - RN_\theta^0\Phi \tag{38}$$

Define $\boldsymbol{\psi} = \left\{\mathbf{q}^{\mathrm{T}}, \mathbf{p}^{\mathrm{T}}\right\}^{\mathrm{T}} = \{u, v, w, \Phi, P_1, P_2, P_3, P_4\}^{\mathrm{T}}$ as a total unknown vector; therefore, Equations (31)–(38) can be rewritten in a matrix form as

$$\dot{\boldsymbol{\psi}} = \mathbf{H}\boldsymbol{\psi} \tag{39}$$

In this manner, Equation (39) can be solved by the method of the separation of variables. Let $\boldsymbol{\psi} = \boldsymbol{\mu}(x)e^{in\theta}$, where n is the circumferential wave number, and $\boldsymbol{\mu}(x)$ is the symplectic eigenfunctions. The eigenvalue equation of Equation (39) can be obtained as

$$\mathrm{H}\boldsymbol{\mu}(x) = n\mathrm{i}\boldsymbol{\mu}(x) \tag{40}$$

The characteristic equation of Equation (40) is

$$\xi^8 + \beta_1\xi^6 + \beta_2\xi^4 + \beta_3\xi^2 + \beta_4 = 0 \tag{41}$$

Obviously, there are eight roots $\xi_i (i = 1, 2, \ldots, 8)$ for Equation (41) and, therefore, the symplectic eigenfunctions can be expressed as

$$\boldsymbol{\mu}(x) = \sum_{i=1}^{8} \mathbf{c}_i e^{\xi_i x} \tag{42}$$

where $\mathbf{c}_i = \left\{c_i^1, c_i^2, \ldots, c_i^8\right\}^T$ are the undetermined coefficient vectors. Here, it should be mentioned that there is only one independent undetermined coefficient vector. The other coefficient vectors can be represented by the coefficient of w, i.e., $\mathbf{c}^3$.

Two types of boundary conditions at $x = 0, L$ are considered, i.e.,

$$\text{Clamped (C)}: \ u = v = w = \frac{\partial w}{\partial x} = 0 \tag{43}$$

$$\text{Simply supported (S)}: \ \frac{\partial u}{\partial x} = v = w = \frac{\partial^2 w}{\partial x^2} = 0 \tag{44}$$

By substituting the symplectic eigenfunctions (42) into the boundary conditions (43) or (44), we have

$$[\mathbf{\Delta}]_{8\times 8}\left(\mathbf{c}^3\right)^{\mathrm{T}} = 0 \tag{45}$$

To obtain the non-trivial solutions of Equation (45), the determinant of the coefficient matrix should be vanished, i.e.,

$$|\mathbf{\Delta}| = 0 \tag{46}$$

After solving Equation (46), the buckling loads are finally obtained, and the minimum buckling load is the critical hydrostatic pressure.

4. Effective Material Properties of Porous GPLRC

The effective material proprieties (Young's modulus E, Poisson's ratio ν, and mass density ρ) of the porous GPLRC are [55]

$$E(z) = E_0[1 - e_0 q(z)] \tag{47}$$

$$\nu(z) = 0.221\widetilde{p} + \nu_0\left(0.342\widetilde{p}^2 - 1.21\widetilde{p} + 1\right) \tag{48}$$

$$\rho(z) = \rho_0[1 - e_m q(z)] \tag{49}$$

where E_0, ν_0, and ρ_0 are the Young's modulus, Poisson's ratio, and mass density of GPLRC without pores, respectively. e_0 is the porosity coefficient. $\widetilde{p} = 1.121\left[1 - \sqrt[2,3]{1 - e_0 q(z)}\right]$ and $e_m = \widetilde{p}/q(z)$. The function $q(z)$ represents the porosity distributions. For the three porosity distributions as shown in Figure 2, $q(z)$ can be expressed as [55].

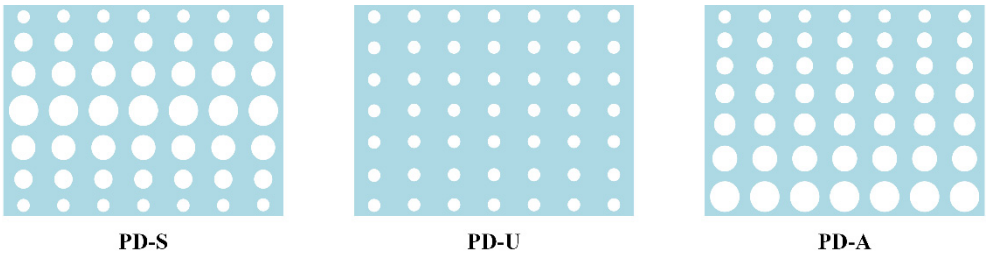

Figure 2. Schematic of porosity distributions.

(i) Symmetric porosity distribution (PD-S):

$$q(z) = \cos\left(\frac{\pi z}{h}\right) \tag{50}$$

(ii) Uniform porosity distribution (PD-U):

$$q(z) = q \tag{51}$$

(iii) Asymmetric porosity distribution (PD-A):

$$q(z) = \cos\left[\frac{\pi}{4}\left(1 + \frac{2z}{h}\right)\right] \tag{52}$$

where $q = \left\{1 - \left[\left(\widetilde{M}/h + 0.121\right)/1.121\right]^{2.3}\right\}/e_0$, and $\widetilde{M} = \int_{-h/2}^{h/2}(1 - \widetilde{p})dz$.

For the three GPL distribution patterns as shown in Figure 3, the volume fraction of GPLs is expressed as [55].

Figure 3. Schematic of GPL dispersion patterns.

(i) Symmetric porosity distribution (GPL-S):

$$V_{GPL} = V_{GPL}^0\left[1 - \cos\left(\frac{\pi z}{h}\right)\right] \tag{53}$$

(ii) Uniform porosity distribution (GPL -U):

$$V_{GPL} = V_{GPL}^0 \tag{54}$$

(iii) Asymmetric porosity distribution (GPL -A):

$$V_{GPL} = V_{GPL}^0\left\{1 - \cos\left[\frac{\pi}{4}\left(1 + \frac{2z}{h}\right)\right]\right\} \tag{55}$$

The weight fraction W_{GPL} and the volume fraction V_{GPL} have the following relation [55]:

$$\frac{W_{GPL}}{W_{GPL} + (1 - W_{GPL})\rho_{GPL}/\rho_M}\int_{-h/2}^{h/2}[1 - e_m q(z)]dz = \int_{-h/2}^{h/2} V_{GPL}[1 - e_m q(z)]dz \tag{56}$$

where W_{GPL} is the weight fraction of the GPLs, ρ_{GPL} and ρ_M are the mass densities of the GPLs and the metal matrix, respectively. By introducing Equations (53)–(55) into Equation (56), the average volume fraction V_{GPL}^0 for different GPL distribution patterns can be calculated, and the corresponding volume fraction V_{GPL} along the thickness can be calculated according to Equations (53)–(55).

The commonly used methods to calculate the effective properties of a nanoparticle-reinforced matrix are the rule of mixture, the modified rule of mixture, the Mori–Tanaka model, the modified Halpin–Tsai model (Rafiee), and the modified Halpin–Tsai model (Yang) [56]. The Halpin–Tsai model modified by Yang et al. gives much more accurate results compared to the experimental data [56]. Therefore, Yang's modified Halpin–Tsai model is used here, and the elastic modulus of GPLRC can be written as [55,56]

$$E_0 = \frac{3}{8}\left(\frac{1+\xi_L^{GPL}\eta_L^{GPL}V_{GPL}}{1-\eta_L^{GPL}V_{GPL}}\right)E_M + \frac{5}{8}\left(\frac{1+\xi_W^{GPL}\eta_W^{GPL}V_{GPL}}{1-\eta_W^{GPL}V_{GPL}}\right)E_M \quad (57)$$

where E_M is the Young's modulus of the metal matrix and

$$\xi_L^{GPL} = \frac{2l_{GPL}}{t_{GPL}},\ \xi_W^{GPL} = \frac{2w_{GPL}}{t_{GPL}},\ \eta_L^{GPL} = \frac{(E_{GPL}/E_M)-1}{(E_{GPL}/E_M)+\xi_L^{GPL}},\ \eta_W^{GPL} = \frac{(E_{GPL}/E_M)-1}{(E_{GPL}/E_M)+\xi_W^{GPL}} \quad (58)$$

in which l_{GPL}, w_{GPL}, and t_{GPL} are the average length, width, and thickness of the GPLs, respectively; E_{GPL} is the Young's modulus of the GPLs.

Using the rule of mixture, the Poisson's ratio ν_0 and mass density ρ_0 of the GPLRC are obtained as [55]

$$\nu_1 = \nu_{GPL}V_{GPL} + \nu_M(1-V_{GPL}) \quad (59)$$

$$\rho_1 = \rho_{GPL}V_{GPL} + \rho_M(1-V_{GPL}) \quad (60)$$

where ν_{GPL} and ν_M are Poisson's ratios of the GPLs and the metal matrix, respectively; ρ_{GPL} and ρ_M are the densities of the GPLs and the metal matrix, respectively.

5. Numerical Results and Discussion

In this section, the critical buckling pressures and buckling mode shapes of ring-stiffened porous GPLRC cylindrical shells under hydrostatic pressure are presented in tabular and graphical forms. Firstly, a comparison study is presented to verify the accuracy of the proposed method. Secondly, the influences of geometric parameters, boundary conditions, ring-stiffeners, and material properties on the buckling behaviors of ring-stiffened porous GPLRC cylindrical shells are discussed. The material properties are taken as: $E_{GPL} = 1010$ GPa, $\nu_{GPL} = 0.186$, $\rho_{GPL} = 1062.5$ kg/m^3, $l_{GPL} = 2.5 \times 10^{-6}$ m, $w_{GPL} = 1.5 \times 10^{-6}$ m, $t_{GPL} = 1.5 \times 10^{-9}$ m, $E_M = 130$ GPa, $\nu_M = 0.34$, and $\rho_M = 8960$ kg/m^3.

5.1. Comparison Study

Since no available results for the buckling of ring-stiffened porous GPLRC cylindrical shells have been reported in the open literature, a homogeneous isotropic ring-stiffened cylindrical shell was considered first. The computation parameters were L = 372.9745 in, h = 1 in, R = 82.1693 in, L_F = 1 in, h_F = 2.306 in, d_F = 0.0638 in, E = 30×10^6 Psi, and ν = 0.3. The comparison of the critical pressures of unstiffened shells and ring-stiffened shells (outside and inside) is presented in Table 1. It was observed that the present results are in good agreement with those of Baruch and Singer [6] and Shen [9], and the maximum error is 1.1023%. There is some error between the present results and the results of Reddy and Starnes [7], which may be due to the difference in theories. Donnell's thin-walled shell theory was used in this study, while Reddy's layerwise theory is used in reference [7]. Subsequently, the variation in the dimensionless critical load parameter $\lambda = PR(1–\nu^2)/(Eh)$ of a homogeneous isotropic ring-stiffened cylindrical shell versus the length-to-radius ratio is plotted in Figure 4, with h/R = 0.01, A_F/h^2 = 4.9152, e/h = 6.2633, I_F/Lh^3 = 0.303457, and ν = 0.3. Good agreements with the existing results [11] are observed again. Finally, an unstiffened nonporous GPLRC cylindrical shell with h = 5 mm, R = 200 mm, W_{GPL} = 0.2, and GPL-U distribution is considered. The variation in the critical pressures versus the length-to-radius ratio is plotted in Figure 5. Clearly, the present results compare well with Shahgholian-Ghahfarokhi's theory and the FEM results [36]. From the above comparisons, it is concluded that the proposed method can accurately predict the critical pressures of ring-stiffened porous GPLRC cylindrical shells under hydrostatic pressure.

Table 1. Critical pressure (Psi) of homogeneous isotropic ring-stiffened cylindrical shells.

	Unstiffened	Ring-Stiffened (Outside)	Ring-Stiffened (Inside)
Present	101.81	325.94	369.99
Baruch and Singer [6]	102	326	370
Deviation with [6]	−0.1863%	−0.0184%	−0.0027%
Reddy and Starnes [7]	93.5	313.7	357.5
Deviation with [7]	8.8877%	3.9018%	3.4937%
Shen [9]	100.7	325.7	368.3
Deviation with [9]	1.1023%	0.0737%	0.4589%

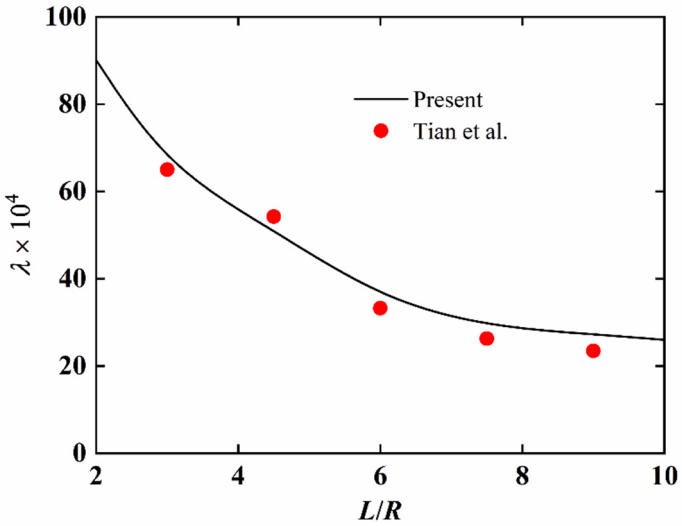

Figure 4. Variation in dimensionless critical load parameter of homogeneous isotropic ring-stiffened cylindrical shells with length–radius ratios [11].

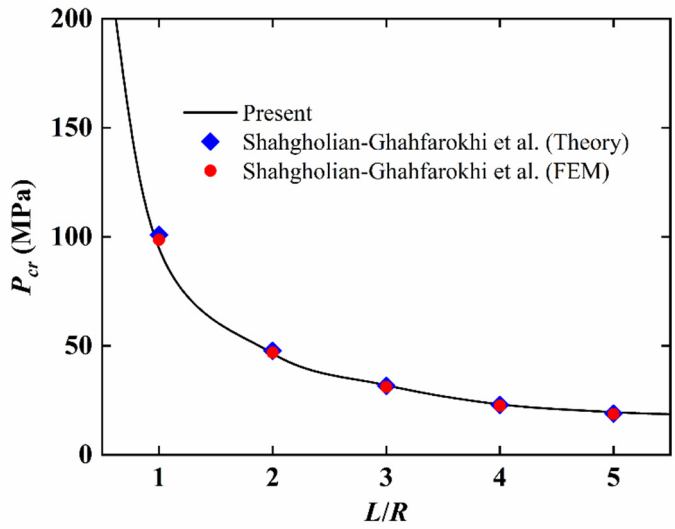

Figure 5. Variation in critical pressure of unstiffened nonporous GPLRC cylindrical shells with length–radius ratios [36].

5.2. Effects of Geometrical Parameters and Boundary Conditions

In this section, the effects of geometrical parameters and boundary conditions on the critical pressures and buckling mode shapes of ring-stiffened porous GPLRC cylindrical shells are investigated. The computation parameters were R = 1 m, W_{GPL} = 1%, e_0 = 0.3, L_F = 0.2 m, h_F = 0.02 m, and d_F = 0.01 m. The porous GPLRC was GPL-S and PD-S. The critical pressure and corresponding circumferential wave number for different boundary conditions, h/R and L/R, are presented in Table 2. It can be observed that the critical pressure increased with the increase in h/R, while it decreased with the increase in L/R. The clamped boundary always led to a greater critical pressure than the simply supported boundary. This is because the constraint degree of the clamped boundary was greater than that of the simply supported boundary. With the increase in L/R, the circumferential wave number decreased gradually. However, h/R had little effect on the circumferential wave number. In addition, the circumferential wave number for the simply supported boundary was usually less than that of the clamped one.

Table 2. Critical pressure of ring-stiffened porous GPLRC cylindrical shells for different boundary conditions, thickness–radius ratios and length–radius ratios.

h/R	*L/R*		
	2	5	10
	C-C		
0.005	1.1606 (6)	0.5262 (4)	0.2795 (3)
0.01	2.5239 (6)	1.1037 (4)	0.5816 (3)
0.02	9.1057 (5)	4.1208 (4)	2.2086 (3)
	S-S		
0.005	0.8966 (5)	0.4069 (3)	0.2351 (2)
0.01	1.9070 (5)	0.8291 (3)	0.4698 (2)
0.02	7.1119 (5)	2.7382 (3)	1.3998 (2)

The variations in the critical pressure with h/R and L/R are shown in Figures 6 and 7, respectively. It can be observed that the variation in the critical pressure for the clamped boundary condition versus h/R or L/R is more pronounced than the simply supported one, and the difference between the two boundary conditions becomes significant for shorter or thicker cylindrical shells. Furthermore, the difference between the unstiffened cylindrical shells and the ring-stiffened cylindrical shells also increased with the increasing h/R and decreasing L/R, which indicates that the reinforcement effect is more obvious for the shorter or thicker cylindrical shell with the same ring-stiffener parameters. Finally, the buckling mode shapes of the ring-stiffened porous GPLRC cylindrical shells for different h/R and L/R values are presented in Figure 8. The above-mentioned influences of the geometrical parameters on the buckling mode shapes can be observed clearly.

5.3. Effects of Material Properties and Ring-Stiffeners

In this section, the effects of the material properties and ring-stiffeners on the buckling behaviors of ring-stiffened porous GPLRC cylindrical shells are revealed. The geometrical parameters were R = 1 m, L/R = 5, h/R = 0.01. The critical pressures for the different GPLs and porosity distributions are tabulated in Tables 3 and 4, respectively. The variations in the critical pressures with various weight fractions and porosity coefficients are plotted in Figures 9 and 10, respectively.

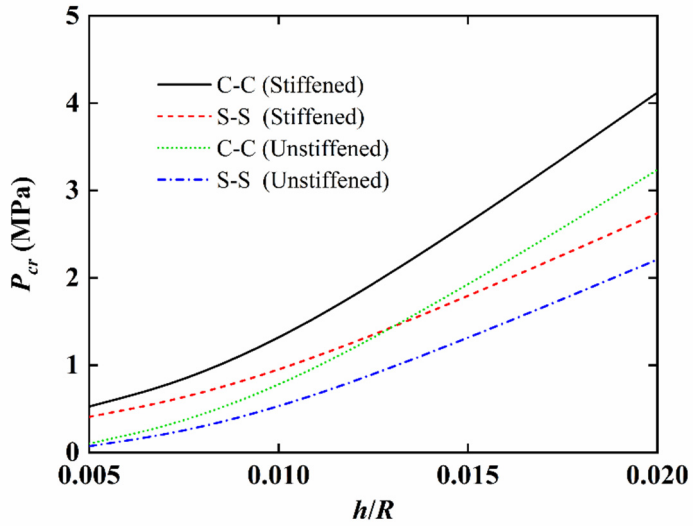

Figure 6. Variation in critical pressure of unstiffened and ring-stiffened porous GPLRC cylindrical shells with thickness–radius ratios.

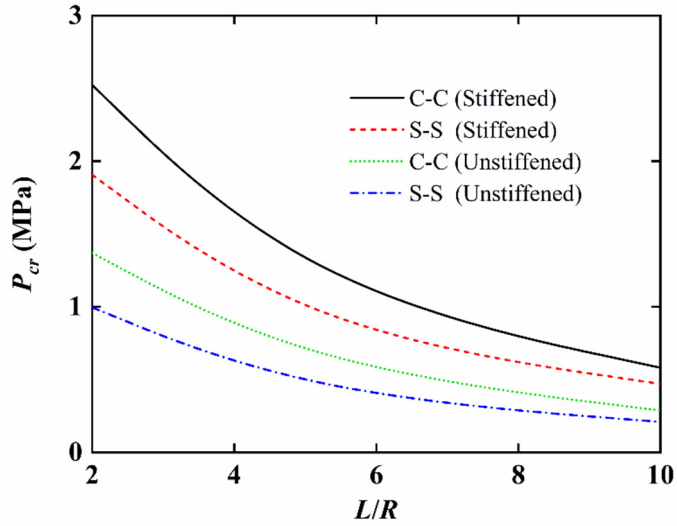

Figure 7. Variation in critical pressure of unstiffened and ring-stiffened porous GPLRC cylindrical shells with length–radius ratios.

It is observed in Table 3 and Figure 9 that the critical pressure increased significantly with the increasing weight fraction of the GPLs, which indicates that adding a small number of GPLs to the metal matrix can significantly improve the anti-buckling performance of the shell. This is because the effective Young's modulus of the composite can be significantly increased by adding GPLs. The GPL-S distribution has the highest critical pressure, and the critical pressure of the GPL-S distribution increased more rapidly with the weight fraction than the GPL-U and GPL-A distributions. This can be explained as the GPL-S distribution has the largest stiffness coefficient.

It can be seen in Table 4 and Figure 10 that the critical pressure decreases with the increasing porosity coefficient. This is because the existence of porosity will reduce the effective Young's modulus of the composite, thus reducing the stability. The PD-S distribution has the highest critical pressure. From the above phenomena, it is concluded that the weight fraction, porosity coefficients, GPLs, and porosity distributions are the key influencing factors on the carrying capacity of ring-stiffened porous GPLRC cylindrical shells, and an optimal design can be achieved by adjusting these parameters.

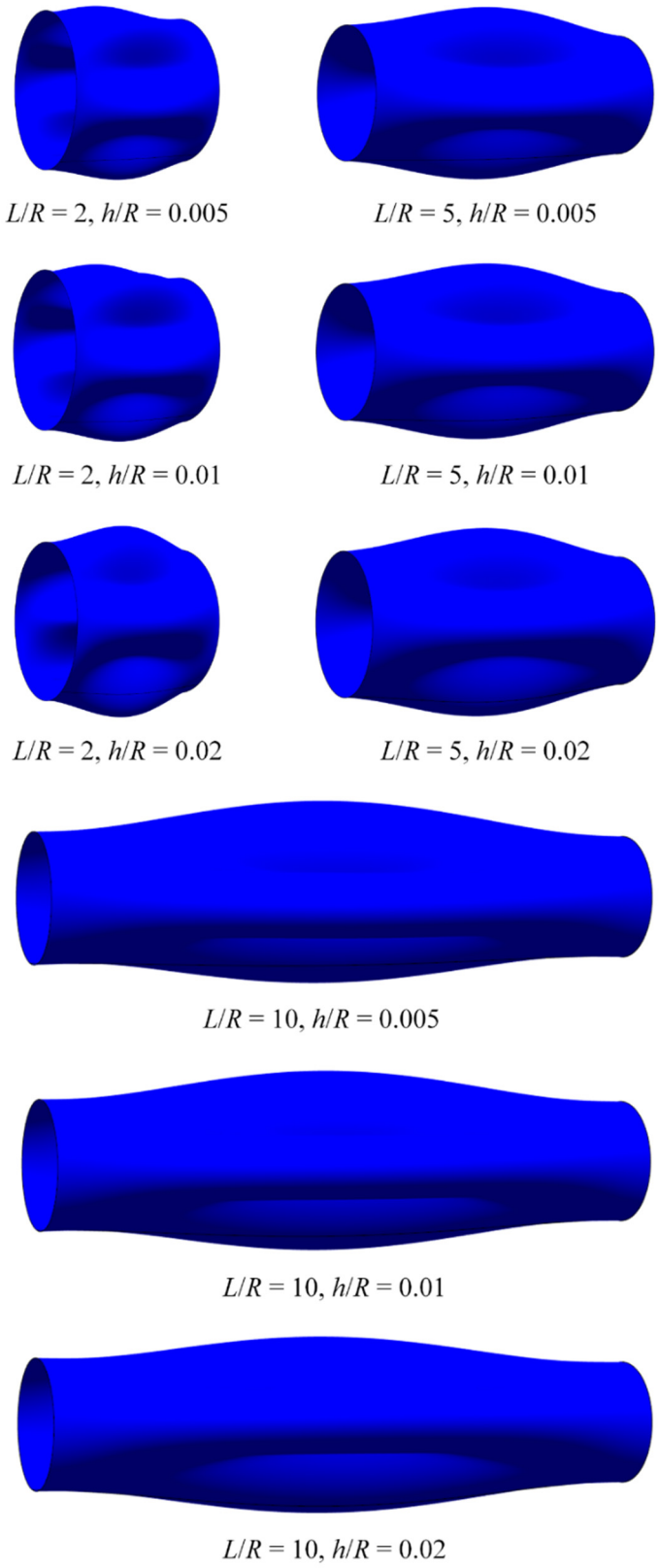

Figure 8. Buckling modes of ring-stiffened porous GPLRC cylindrical shells for different thickness–radius ratios and length–radius ratios.

Table 3. Critical pressure of ring-stiffened porous GPLRC cylindrical shells for different weight fractions and GPL distributions.

	W_{GPL} = 0	0.5%	1%	1.5%	2%
	PD-S				
GPL-S	0.8394	0.9786	1.1037	1.2180	1.3232
GPL-U	0.8394	0.9404	1.0312	1.1143	1.1908
GPL-A	0.8394	0.9102	0.9747	1.0344	1.0899
	PD-U				
GPL-S	0.8200	0.9491	1.0652	1.1714	1.2692
GPL-U	0.8200	0.9161	1.0023	1.0811	1.1537
GPL-A	0.8200	0.8884	0.9512	1.0094	1.0638
	PD-A				
GPL-S	0.8022	0.9288	1.0437	1.1494	1.2471
GPL-U	0.8022	0.8982	0.9845	1.0635	1.1364
GPL-A	0.8022	0.8715	0.9354	0.9949	1.0504

Table 4. Critical pressure of ring-stiffened porous GPLRC cylindrical shells for different porosity coefficients and porosity distributions.

	e_0 = 0.1	0.2	0.3	0.4	0.5
	GPL-S				
PD-S	1.1742	1.1392	1.1037	1.0678	1.0311
PD-U	1.1617	1.1138	1.0652	1.0158	0.9650
PD-A	1.1558	1.1008	1.0437	0.9840	0.9209
	GPL-U				
PD-S	1.0976	1.0645	1.0312	0.9977	0.9639
PD-U	1.0883	1.0456	1.0023	0.9581	0.9127
PD-A	1.0832	1.0347	0.9845	0.9323	0.8774
	GPL-A				
PD-S	1.0439	1.0095	0.9747	0.9395	0.9038
PD-U	1.0363	0.9940	0.9512	0.9076	0.8629
PD-A	1.0316	0.9841	0.9354	0.8851	0.8328

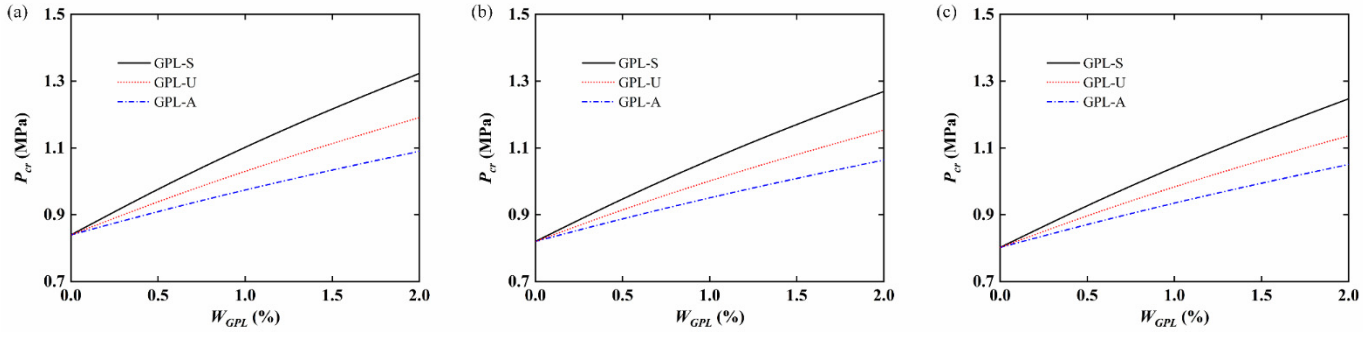

Figure 9. Variations in critical pressure of ring-stiffened porous GPLRC cylindrical shells with weight fractions for different GPLs distributions (**a**): PD-S; (**b**): PD-U; (**c**): PD-A.

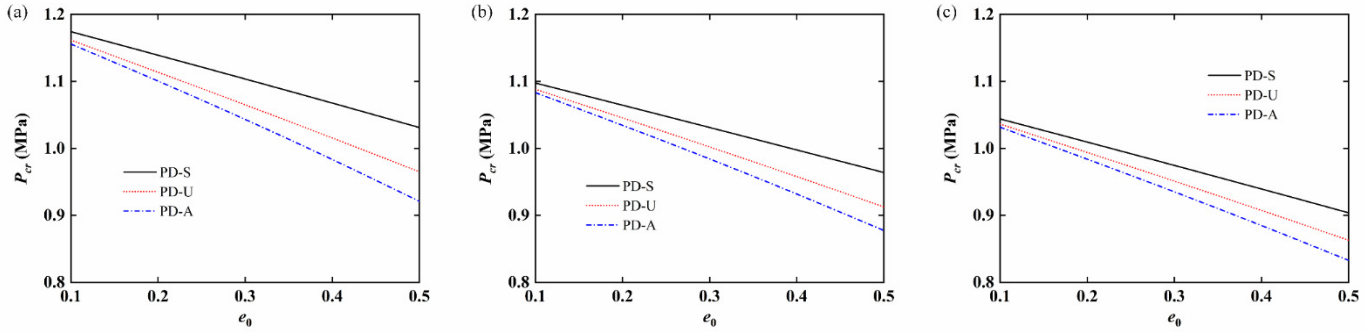

Figure 10. Variations in critical pressure of ring-stiffened porous GPLRC cylindrical shells with porosity coefficients for different porosity distributions (**a**): GPL-S; (**b**): GPL-U; (**c**): GPL-A.

Figure 11 shows the variation in the critical pressure with the length-to-thickness ratio l_{GPL}/t_{GPL} of the GPLs under different length-to-width ratios l_{GPL}/w_{GPL} of the GPLs. It can be observed that the critical pressure first increased with the increase in the l_{GPL}/t_{GPL}, and then tended to remain unchanged. The critical pressure of ring-stiffened porous GPLRC cylindrical shells was higher for the lower length-to-width ratios l_{GPL}/w_{GPL}.

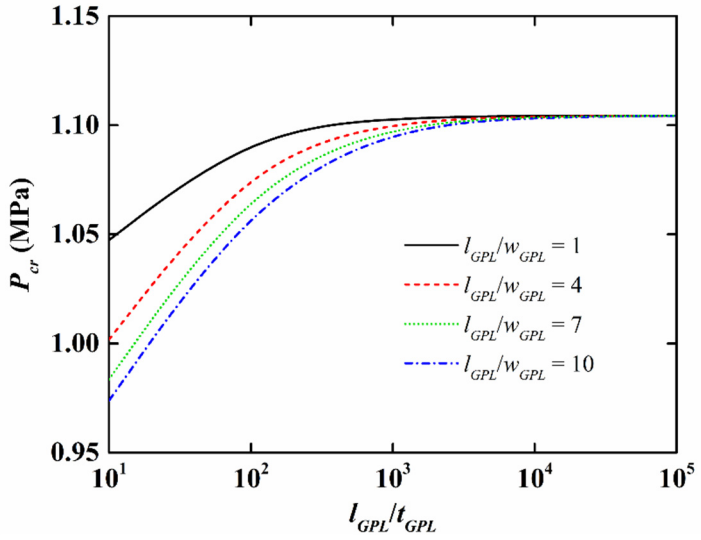

Figure 11. Variation in critical pressure of ring-stiffened porous GPLRC cylindrical shells with porosity coefficients for different porosity distributions.

The variations in the critical pressures with various ring-stiffener heights (d_F/h_F = 0.5) and ring-stiffener spacings are presented in Figures 12 and 13, respectively. It can be observed in Figure 12 that with the increase in the ring-stiffener size, the critical pressure increased and the slope of the curves also increased. It is seen in Figure 13 that the critical pressure and the slope of the curves decreased with the increasing ring-stiffener spacing. This is because increasing the ring-stiffener size or reducing the ring-stiffener spacing will increase the equivalent stiffness coefficient.

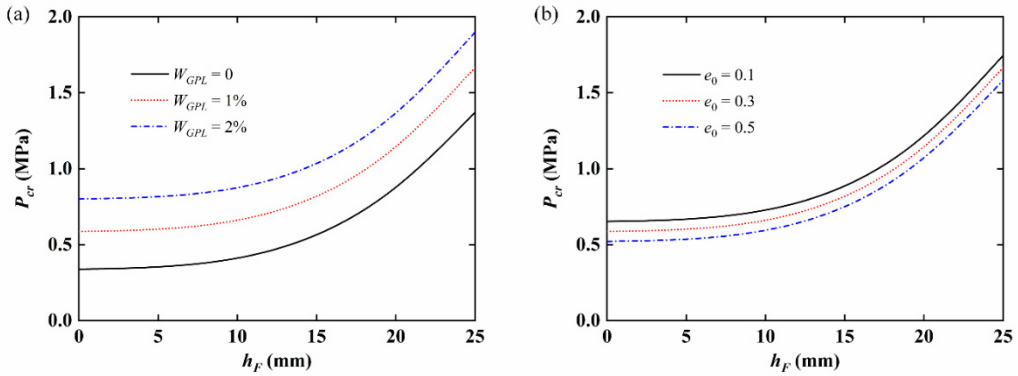

Figure 12. Variations in critical pressure of ring-stiffened porous GPLRC cylindrical shells with ring-stiffener height for different (**a**) weight fractions and (**b**) porosity coefficients.

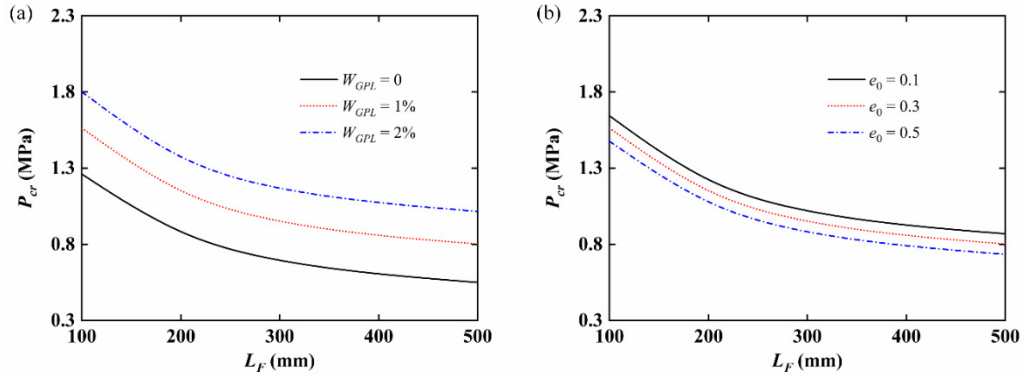

Figure 13. Variations in critical pressure of ring-stiffened porous GPLRC cylindrical shells with ring-stiffener spacing for different (**a**) weight fractions and (**b**) porosity coefficients.

6. Conclusions

An analytical buckling analysis of ring-stiffened porous GPLRC cylindrical shells subjected to hydrostatic pressure was performed by a novel symplectic approach. The governing equation in the Hamiltonian form was obtained by introducing a new total unknown vector, and therefore, it could be solved by the method of the separation of variables. In this manner, accurate critical pressures and analytical buckling mode shapes were obtained simultaneously. Numerical examples verify the accuracy of the proposed method, and the effects of the key influencing parameters on the buckling behavior are discussed in detail. The main conclusions are as follows:

(i) The geometrical parameters are major influencing factors on the critical pressures and buckling mode shapes. The critical pressure increases with an increasing h/R and decreases with an increasing L/R. The circumferential wave number decreases with an increasing L/R and remains basically unchanged with a change in h/R;

(ii) The stability of ring-stiffened cylindrical shells can be significantly improved by adding a small number of GPLs to the metal matrix. The critical pressure increases with an increasing weight fraction and decreases with an increasing porosity coefficient. The GPL-S and PD-S distributions have the highest critical pressure.

(iii) The ring-stiffeners can also significantly improve the stability, and the stability performance is stronger when the ring-stiffener size is larger and the ring-stiffener spacing is smaller. Under the specific ring-stiffener parameters, the reinforcement is more significant for shorter or thicker porous GPLRC cylindrical shells.

The theoretical model, solution method, and new observations can provide a theoretical basis for the stability analysis of stiffened composite cylindrical shells. The obtained analytical solutions can also be used as the design specifications of underwater pressure

structures, and they are helpful for the design of military submarines, underwater pipelines, and other marine equipment.

Author Contributions: Conceptualization, Z.S. and J.S.; methodology, Z.S. and J.S.; software, G.H. and X.N.; validation, G.H.; formal analysis, G.H.; investigation, Z.S.; resources, Z.S. and J.S.; data curation, X.N.; writing—original draft preparation, Z.S.; writing—review and editing, J.S.; visualization, G.H. and X.N.; supervision, J.S.; funding acquisition, J.S. All authors have read and agreed to the published version of the manuscript.

Funding: This research was funded by the Fundamental Research Funds for the Central Universities, grant number DUT22LK16.

Institutional Review Board Statement: Not applicable.

Informed Consent Statement: Not applicable.

Data Availability Statement: The data presented in this study are available on request from the corresponding author.

Conflicts of Interest: The authors declare no conflict of interest.

References

1. Cho, S.R.; Muttaqie, T.; Do, Q.T.; Kim, S.; Kim, S.M.; Han, D.H. Experimental investigations on the failure modes of ring-stiffened cylinders under external hydrostatic pressure. *Int. J. Nav. Archit. Ocean Eng.* **2018**, *10*, 711–729. [CrossRef]
2. Kendrick, S. The Buckling under External Pressure of Circular Cylindrical Shells with Evenly Spaced, Equal Strength, Circular Ring Frames. Part II; Naval Construction Research Establishment Report NCRE/R No. 244. 1953. Available online: https://www.osti.gov/biblio/4304774 (accessed on 28 September 2022).
3. Bryant, A.R. Hydrostatic Pressure Buckling of a Ring-Stiffened Tube; Naval Construction Research Establishment Report NCRE/R No. 306. 1954. Available online: https://discovery.nationalarchives.gov.uk/details/r/C4124221 (accessed on 28 September 2022).
4. Galletly, G.D.; Slankard, R.C.; Wenk, E., Jr. General instability of ring-stiffened cylindrical shells subject to external hydrostatic pressure-A comparison of theory and experiment. *J. Appl. Mech.* **1958**, *25*, 259–266. [CrossRef]
5. Yamamoto, Y.; Homma, Y.; Oshima, K.; Mishiro, Y.; Terada, H.; Yoshikawa, T.; Morihana, H.; Yamauchi, Y.; Takenaka, M. General instability of ring-stiffened cylindrical shells under external pressure. *Mar. Struct.* **1989**, *2*, 133–149. [CrossRef]
6. Rathinam, N.; Prabu, B.; Anbazhaghan, N. Buckling analysis of ring stiffened thin cylindrical shell under external pressure. *J. Ocean Eng. Sci.* **2021**, *6*, 360–366. [CrossRef]
7. Baruch, M.; Singer, J. Effect of eccentricity of stiffeners on the general instability of stiffened cylindrical shells under hydrostatic pressure. *J. Mech. Eng. Sci.* **1963**, *5*, 23–27. [CrossRef]
8. Reddy, J.N.; Starnes, J.H. General buckling of stiffened circular cylindrical shells according to a layerwise theory. *Comput. Struct.* **1993**, *49*, 605–616. [CrossRef]
9. Shen, H.S.; Zhou, P.; Chen, T.Y. Postbuckling analysis of stiffened cylindrical shells under combined external pressure and axial compression. *Thin-Walled Struct.* **1993**, *15*, 43–63. [CrossRef]
10. Shen, H.S. Postbuckling analysis of imperfect stiffened laminated cylindrical shells under combined external pressure and thermal loading. *Int. J. Mech. Sci.* **1998**, *40*, 339–355. [CrossRef]
11. Tian, J.; Wang, C.M.; Swaddiwudhipong, S. Elastic buckling analysis of ring-stiffened cylindrical shells under general pressure loading via the Ritz method. *Thin-Walled Struct.* **1999**, *35*, 1–24. [CrossRef]
12. Ghorbanpour Arani, A.; Loghman, A.; Mosallaie Barzoki, A.A.; Kolahchi, R. Elastic buckling analysis of ring and stringer-stiffened cylindrical shells under general pressure and axial compression via the Ritz method. *J. Solid Mech.* **2010**, *2*, 332–347.
13. Yang, Y.; Li, J.J.; Zhang, Y.; He, Q.; Dai, H.L. A semi-analytical analysis of strength and critical buckling behavior of underwater ring-stiffened cylindrical shells. *Eng. Struct.* **2021**, *227*, 111396. [CrossRef]
14. Dung, D.V.; Hoa, L.K. Nonlinear buckling and post-buckling analysis of eccentrically stiffened functionally graded circular cylindrical shells under external pressure. *Thin-Walled Struct.* **2013**, *63*, 117–124. [CrossRef]
15. Dai, H.L.; Qi, L.L.; Zheng, H.Y. Buckling analysis for a ring-stiffened FGM cylindrical shell under hydrostatic pressure and thermal loads. *J. Mech.* **2014**, *30*, 403–410. [CrossRef]
16. Phuong, N.T.; Trung, N.T.; Van Doan, C.; Thang, N.D.; Duc, V.M.; Nam, V.H. Nonlinear thermomechanical buckling of FG-GRC laminated cylindrical shells stiffened by FG-GRC stiffeners subjected to external pressure. *Acta Mech.* **2020**, *231*, 5125–5144. [CrossRef]
17. Arshid, E.; Arshid, H.; Amir, S.; Mousavi, S.B. Free vibration and buckling analyses of FG porous sandwich curved microbeams in thermal environment under magnetic field based on modified couple stress theory. *Arch. Civ. Mech. Eng.* **2021**, *21*, 1–23. [CrossRef]

18. Arshid, E.; Khorasani, M.; Soleimani-Javid, Z.; Amir, S.; Tounsi, A. Porosity-dependent vibration analysis of FG microplates embedded by polymeric nanocomposite patches considering hygrothermal effect via an innovative plate theory. *Eng. Comput.* **2021**, 1–22. [CrossRef]
19. Arshid, E.; Amir, S.; Loghman, A. Static and dynamic analyses of FG-GNPs reinforced porous nanocomposite annular micro-plates based on MSGT. *Int. J. Mech. Sci.* **2020**, *180*, 105656. [CrossRef]
20. Arshid, E.; Amir, S.; Loghman, A. Thermal buckling analysis of FG graphene nanoplatelets reinforced porous nanocomposite MCST-based annular/circular microplates. *Aerosp. Sci. Technol.* **2021**, *111*, 106561. [CrossRef]
21. Khorasani, M.; Soleimani-Javid, Z.; Arshid, E.; Lampani, L.; Civalek, Ö. Thermo-elastic buckling of honeycomb micro plates integrated with FG-GNPs reinforced Epoxy skins with stretching effect. *Compos. Struct.* **2021**, *258*, 113430. [CrossRef]
22. Mousavi, S.B.; Amir, S.; Jafari, A.; Arshid, E. Analytical solution for analyzing initial curvature effect on vibrational behavior of PM beams integrated with FGP layers based on trigonometric theories. *Adv. Nano Res.* **2021**, *10*, 235–251.
23. Liu, P.W.; Jin, Z.; Katsukis, G.; Drahushuk, L.W.; Shimizu, S.; Shih, C.J.; Wetzel, E.D.; Taggart-Scarff, J.K.; Qing, B.; Van Vliet, K.J.; et al. Layered and scrolled nanocomposites with aligned semi-infinite graphene inclusions at the platelet limit. *Science* **2016**, *353*, 364–367. [CrossRef] [PubMed]
24. Zhang, Y.Y.; Li, X.D. Bioinspired, graphene/Al2O3 doubly reinforced Aluminum composites with high strength and toughness. *Nano Lett.* **2017**, *17*, 6907–6915. [CrossRef] [PubMed]
25. Nieto, A.; Bisht, A.; Lahiri, D.; Zhang, C.; Agarwal, A. Graphene reinforced metal and ceramic matrix composites: A review. *Int. Mater. Rev.* **2017**, *62*, 241–302. [CrossRef]
26. Papageorgiou, D.G.; Kinloch, I.A.; Young, R.J. Mechanical properties of graphene and graphene-based nanocomposites. *Prog. Mater. Sci.* **2017**, *90*, 75–127.
27. Young, R.J.; Liu, M.F.; Kinloch, I.A.; Li, S.H.; Zhao, X.; Vallés, C.; Papageorgiou, D.G. The mechanics of reinforcement of polymers by graphene nanoplatelets. *Compos. Sci. Technol.* **2018**, *154*, 110–116. [CrossRef]
28. Ahmad, S.R.; Xue, C.Z.; Young, R.J. The mechanisms of reinforcement of polypropylene by graphene nanoplatelets. *Mater. Sci. Eng. B* **2017**, *216*, 2–9. [CrossRef]
29. Liu, D.Y.; Kitipornchai, S.; Chen, W.Q.; Yang, J. Three-dimensional buckling and free vibration analyses of initially stressed functionally graded graphene reinforced composite cylindrical shell. *Compos. Struct.* **2018**, *189*, 560–569. [CrossRef]
30. Zhao, Z.; Ni, Y.W.; Zhu, S.B.; Tong, Z.Z.; Zhang, J.L.; Zhou, Z.H.; Lim, C.W.; Xu, X.S. Thermo-electro-mechanical size-dependent buckling response for functionally graded graphene platelet reinforced piezoelectric cylindrical nanoshells. *Int. J. Struct. Stab. Dyn.* **2020**, *20*, 2050100. [CrossRef]
31. Sun, J.B.; Ni, Y.W.; Gao, H.Y.; Zhu, S.B.; Tong, Z.Z.; Zhou, Z.H. Torsional buckling of functionally graded multilayer graphene nanoplatelet-reinforced cylindrical shells. *Int. J. Struct. Stab. Dyn.* **2019**, *20*, 2050005. [CrossRef]
32. Zhou, Z.H.; Ni, Y.W.; Tong, Z.Z.; Zhu, S.B.; Sun, J.B.; Xu, X.S. Accurate nonlinear buckling analysis of functionally graded porous graphene platelet reinforced composite cylindrical shells. *Int. J. Mech. Sci.* **2019**, *151*, 537–550. [CrossRef]
33. Dong, Y.H.; He, L.W.; Wang, L.; Li, Y.H.; Yang, J. Buckling of spinning functionally graded graphene reinforced porous nanocomposite cylindrical shells: An analytical study. *Aerosp. Sci. Technol.* **2018**, *82–83*, 466–478. [CrossRef]
34. Sun, J.B.; Zhu, S.B.; Tong, Z.Z.; Zhou, Z.H.; Xu, X.S. Post-buckling analysis of functionally graded multilayer graphene platelet reinforced composite cylindrical shells under axial compression. *Proc. R. Soc. A Math. Phys. Eng. Sci.* **2020**, *476*, 20200506. [CrossRef] [PubMed]
35. Blooriyan, S.; Ansari, R.; Darvizeh, A.; Gholami, R.; Rouhi, H. Postbuckling analysis of functionally graded graphene platelet-reinforced polymer composite cylindrical shells using an analytical solution approach. *Appl. Math. Mech.* **2019**, *40*, 1001–1016. [CrossRef]
36. Shahgholian-Ghahfarokhi, D.; Rahimi, G.; Khodadadi, A.; Salehipour, H.; Afrand, M. Buckling analyses of FG porous nanocomposite cylindrical shells with graphene platelet reinforcement subjected to uniform external lateral pressure. *Mech. Based Des. Struct. Mach.* **2021**, *49*, 1059–1079. [CrossRef]
37. Shahgholian-Ghahfarokhi, D.; Safarpour, M.; Rahimi, A.R.; Alibeigloo, A. Buckling analyses of functionally graded graphene-reinforced porous cylindrical shell using the Rayleigh-Ritz method. *Acta Mech.* **2020**, *231*, 1887–1902. [CrossRef]
38. Shahgholian-Ghahfarokhi, D.; Safarpour, M.; Rahimi, A.R. Torsional buckling analyses of functionally graded porous nanocomposite cylindrical shells reinforced with graphene platelets (GPLs). *Mech. Based Des. Struct. Mach.* **2021**, *49*, 81–102. [CrossRef]
39. Wang, Y.; Feng, C.; Zhao, Z.; Yang, J. Buckling of graphene platelet reinforced composite cylindrical shell with cutout. *Int. J. Struct. Stab. Dyn.* **2017**, *18*, 1850040. [CrossRef]
40. Wang, Y.; Feng, C.; Zhao, Z.; Yang, J. Eigenvalue buckling of functionally graded cylindrical shells reinforced with graphene platelets (GPL). *Compos. Struct.* **2018**, *202*, 38–46. [CrossRef]
41. Wang, Y.; Feng, C.; Zhao, Z.; Lu, F.Z.; Yang, J. Torsional buckling of graphene platelets (GPLs) reinforced functionally graded cylindrical shell with cutout. *Compos. Struct.* **2018**, *197*, 72–79. [CrossRef]
42. Yao, W.A.; Zhong, W.X.; Lim, C.W. *Symplectic Elasticity*; World Scientific: Singapore, 2009.
43. Lim, C.W.; Xu, X.S. Symplectic elasticity: Theory and applications. *Appl. Mech. Rev.* **2010**, *63*, 050802. [CrossRef]
44. Arshid, E.; Khorshidvand, A.R. Free vibration analysis of saturated porous FG circular plates integrated with piezoelectric actuators via differential quadrature method. *Thin-Walled Struct.* **2018**, *125*, 220–233. [CrossRef]

45. Arshid, E.; Amir, S.; Loghman, A. Bending and buckling behaviors of heterogeneous temperature-dependent micro annular/circular porous sandwich plates integrated by FGPEM nano-Composite layers. *J. Sandw. Struct. Mater.* **2021**, *23*, 3836–3877. [CrossRef]
46. Arshid, E.; Kiani, A.; Amir, S. Magneto-electro-elastic vibration of moderately thick FG annular plates subjected to multi physical loads in thermal environment using GDQ method by considering neutral surface. *Proc. Inst. Mech. Eng. Part L J. Mater. Des. Appl.* **2019**, *233*, 2140–2159. [CrossRef]
47. Arshid, E.; Soleimani-Javid, Z.; Amir, S.; Duc, N.D. Higher-order hygro-magneto-electro-thermomechanical analysis of FG-GNPs-reinforced composite cylindrical shells embedded in PEM layers. *Aerosp. Sci. Technol.* **2022**, *126*, 107573. [CrossRef]
48. Amir, S.; Arshid, E.; Rasti-Alhosseini, S.M.A.; Loghman, A. Quasi-3D tangential shear deformation theory for size-dependent free vibration analysis of three-layered FG porous micro rectangular plate integrated by nano-composite faces in hygrothermal environment. *J. Therm. Stress.* **2020**, *43*, 133–156. [CrossRef]
49. Arshid, E.; Kiani, A.; Amir, S.; Dehaghani, M.Z. Asymmetric free vibration analysis of first-order shear deformable functionally graded magneto-electro-thermo-elastic circular plates. *Proc. Inst. Mech. Eng. Part C J. Mech. Eng. Sci.* **2019**, *233*, 5659–5675. [CrossRef]
50. Soleimani-Javid, Z.; Arshid, E.; Amir, S.; Bodaghi, M. On the higher-order thermal vibrations of FG saturated porous cylindrical micro-shells integrated with nanocomposite skins in viscoelastic medium. *Def. Technol.* **2022**, *18*, 1416–1434. [CrossRef]
51. Khorasani, M.; Soleimani-Javid, Z.; Arshid, E.; Amir, S.; Civalek, Ö. Vibration analysis of graphene nanoplatelets' reinforced composite plates integrated by piezo-electromagnetic patches on the piezo-electromagnetic media. *Waves Random Complex Media* **2021**, 1–31. [CrossRef]
52. Amir, S.; Arshid, E.; Maraghi, Z.K.; Loghman, A.; Ghorbanpour Arani, A. Vibration analysis of magnetorheological fluid circular sandwich plates with magnetostrictive facesheets exposed to monotonic magnetic field located on visco-Pasternak substrate. *J. Vib. Control* **2020**, *26*, 1523–1537. [CrossRef]
53. Mohammadimehr, M.; Arshid, E.; Rasti-Alhosseini, S.M.A.; Amir, S.; Arani, M.R.G. Free vibration analysis of thick cylindrical MEE composite shells reinforced CNTs with temperature-dependent properties resting on viscoelastic foundation. *Struct. Eng. Mech.* **2019**, *70*, 683–702.
54. Lai, A.D.; Jia, J.F.; Qu, J.L.; Wang, J.Y.; Sun, J.B.; Zhou, Z.H.; Xu, X.S.; Lim, C.W. Local-global buckling of cylindrical shells with wall thinning defects. *Mech. Based Des. Struct. Mach.* **2021**, 1–20. [CrossRef]
55. Kitipornchai, S.; Chen, D.; Yang, J. Free vibration and elastic buckling of functionally graded porous beams reinforced by graphene platelets. *Mater. Des.* **2017**, *116*, 656–665. [CrossRef]
56. Zhao, S.Y.; Zhao, Z.; Yang, Z.C.; Ke, L.L.; Kitipornchai, S.; Yang, J. Functionally graded graphene reinforced composite structures: A review. *Eng. Struct.* **2020**, *210*, 110339. [CrossRef]